



Article

Laser Machining of Nickel Oxide–Yttria Stabilized Zirconia Composite for Surface Modification in Solid Oxide Fuel Cells

Miguel Morales ^{1,2,*} , Sandra García-González ^{1,2}, Michaela Plch ^{1,2}, Dario Montinaro ³ and Emilio Jiménez-Piqué ^{1,2} 

¹ CIEFMA—Department of Materials Science and Engineering, EEBE—Campus Diagonal Besòs, Universitat Politècnica de Catalunya—BarcelonaTech, C/Eduard Maristany, 16, 08019 Barcelona, Spain; sandra.garcia@upc.edu (S.G.-G.); michaela.plch99@gmail.com (M.P.); emilio.jimenez@upc.edu (E.J.-P.)

² Barcelona Research Center in Multiscale Science and Engineering,

Universitat Politècnica de Catalunya—BarcelonaTech, C/Eduard Maristany, 16, 08019 Barcelona, Spain

³ SolydEra SpA, Viale Trento 115/117, 38017 Mezzolombardo, TN, Italy; dario.montinaro@solydera.com

* Correspondence: miguel.morales-comas@upc.edu

Abstract: Laser machining of the nickel oxide–yttria-stabilized zirconia (NiO–YSZ) composite in Solid Oxide Fuel Cells (SOFCs) may be an effective approach to enlarge the electrode–electrolyte interface and improve the cell performance. However, laser energy can cause thermal damage to the composite surface during the machined operation. In this work, the microstructure changes and the collateral damage caused by pulsed laser machining on the sintered NiO–YSZ of the state-of-the-art SOFCs were evaluated using complementary analysis techniques. Laser patterns consisting of parallel tracks on sintered NiO–YSZ were processed, varying the laser parameters such as frequency and laser beam energy density. The analyses evidenced a heat-affected zone (HAZ) limited to around 2 μm with microcracking, porosity reduction, and recrystallization. The changes in chemical composition, phase transformation of YSZ and mechanical properties at the machined surface were quite limited.

Keywords: solid oxide fuel cells; laser machining; nickel oxide–yttria-stabilized zirconia; composite; anode; corrugated surface; surface damage



Citation: Morales, M.; García-González, S.; Plch, M.; Montinaro, D.; Jiménez-Piqué, E. Laser Machining of Nickel Oxide–Yttria Stabilized Zirconia Composite for Surface Modification in Solid Oxide Fuel Cells. *Crystals* **2023**, *13*, 1016. <https://doi.org/10.3390/cryst13071016>

Academic Editors: Fengyu Shen and Yucun Zhou

Received: 29 May 2023
Revised: 21 June 2023
Accepted: 22 June 2023
Published: 26 June 2023



Copyright: © 2023 by the authors. Licensee MDPI, Basel, Switzerland. This article is an open access article distributed under the terms and conditions of the Creative Commons Attribution (CC BY) license (<https://creativecommons.org/licenses/by/4.0/>).

1. Introduction

In recent decades, numerous strategies for improving the performance and reliability of Solid Oxide Fuel Cells (SOFCs) have been proposed, e.g., from the cell configuration [1–3] to the improvements in the materials used as electrolyte and electrodes [4,5], among others. In the case of fuel electrode, the state-of-the-art material is composed of nickel-based yttria-stabilized zirconia (Ni–YSZ). The optimization of the several microstructure parameters in the electrode—such as the percentage of electrode constituents [6,7], the tortuosity [8–10], the three-phase boundaries (TPBs) [11,12], and the porosity of Ni–YSZ support [13–16]—has significantly improved the power density of SOFCs. More recently, many works have reported enhancements at the electrode–electrolyte interfaces, because the conventional interfaces cause a remarkable increase to the total ohmic and polarization resistances of SOFCs [17]. An effective approach for reducing the interfacial resistance is to increase the electrode–electrolyte interface area. In this regard, micro-patterning processes based on conventional ceramic technologies—such as powder metallurgy [18], spray deposition of YSZ particles [19], and mesh pressing of tape-casted sheets [20,21]—have been developed. Alternatively, advanced processing techniques—such as atmospheric plasma spraying [22], thermal spray [23], micro-powder imprinting method [24], inkjet printing techniques [25,26], lithography [27,28] and stereolithography [29,30]—allowed us to obtain highly complex electrode–electrolyte interfaces with excellent control and reproducibility.

Within the above framework, laser machining has emerged as an effective method for enlarging the electrode–electrolyte contact area in a controlled, flexible, and reproducible

manner [31]. Another positive point of this approach is the incorporation of the laser machining step into the typical cell processing, maintaining the state-of-the-art material components and techniques already proven in the SOFC field. For the electrolyte-supported cell configuration, Cebollero et al. engraved square arrays with a lattice parameter of 28 μm and a depth up to 7 μm on YSZ [32] and hexagonal arrangements of ~ 22 μm depth with 24 μm lattice parameter [33], significantly reducing their polarization resistance at the oxygen electrode–electrolyte interface. The same researchers also processed thin self-supported YSZ electrolytes to decrease strongly the ohmic resistance [34]. Using the same approach, Cai et al. [35] employed laser micro-processing on the electrolyte-supported surfaces in order to modify the electrolytes with windows-like and dimples-like array structures with 12–27 μm depth and 38–60 μm diameter. Other researchers proposed to increase the electrode–electrolyte contact area using laser-machining on the NiO–YSZ fuel electrode, which is particularly interesting for the current state-of-the-art anode-supported SOFCs. In this regard, the 2D and 3D numerical simulation studies of Konno et al. [36], Seo et al. [37] and Jin et al. [38] demonstrated that the surface enlargement with a wavy electrode–electrolyte interface is the most effective way for an anode-supported cell. Zhang et al. [39] reported an increase of 55% in power density with a wavy interface based on the pits array (80 μm depth and 110–160 μm diameter) in the NiO–YSZ anode. Furthermore, laser drilling of cylindrical hole patterns in porous Ni–YSZ cermet was implemented by Gorauskis et al. [40] and Gu et al. [41]. These researchers successfully fabricated straight open finger-like pores to increase the gas transport along the fuel electrode, thereby reducing the concentration polarization of SOFCs.

Compared to other advanced and conventional ceramic techniques, laser machining may present much higher flexibility, precision and reproducibility. However, it presents a relevant issue related to the process effectivity and quality of the laser-machined surface, because this technique usually involves a combination of photochemical evaporation and photothermal melt expulsion [42,43]. The effectivity of laser machining mainly depends on input process parameters such as beam characteristics (pulse energy, pulse width, duration and the number of pulses, beam quality, wavelength); laser characteristics (laser power, focal distance, focal distance, assist gas pressure, nozzle diameter); and drilling characteristics (angle, depth and diameter of drilling) [43–46]. The laser machining process usually causes damage to the substrate around the laser pattern. Thus, the output performance properties of laser ablation must be analyzed after laser treatment, and mainly depends on the quality characteristics (material removal rate, surface roughness, etc.); geometrical characteristics (hole/track taper, circularity . . .); microstructure characteristics (spatter formation, recast layer thickness, thermal damage, heat affected zone (HAZ), microcracks . . .) [47,48]. Previous works reported that the ablation rate of sintered NiO–YSZ substrate is lower than that of the green state of NiO–YSZ [40,49,50]. Meanwhile, the laser ablation of Ni–YSZ cermet results in a poor-quality surface. Using the optimized laser ablation parameters, the green NiO–YSZ substrates were machined to desired structures without significant changes within the microstructure of the final Ni–YSZ cermet. Despite the clear advantages of laser ablation on unsintered NiO–YSZ, some processing routes for the state-of-the-art and future SOFC generations could require post-processing treatments, using laser machining on pre-sintered or sintered NiO–YSZ. For these cases, it would be very interesting to know the effects of laser machining technology on the sintered substrate. Unfortunately, detailed damage evaluation of laser treatment in sintered NiO–YSZ is scarce in the literature. Following the above idea, the authors of this study have reported several studies about the microstructure changes caused by laser patterning in dental-grade zirconia [51–53] and recently YSZ for SOFC applications [54].

This work aimed to evaluate the damage produced by laser machining on sintered NiO–YSZ composites, focusing on the changes in surface topography, chemical composition, microstructure and mechanical properties. For this purpose, sintered NiO–YSZ substrates of SOFCs fabricated using industrially scalable techniques (i.e., tape casting) were machined under distinct laser machining conditions to obtain linear patterns. The surface of the laser-machined NiO–YSZ substrates was characterized using complementary microanalysis

and microscopy techniques. Additionally, special attention was paid to the study of the mechanical properties at the scale of the NiO–YSZ microstructure using the instrumented Nanoindentation technique, as these properties could be critical for the functionality and structural integrity of machined NiO–YSZ anode-supported cells.

2. Materials and Methods

2.1. Preparation of NiO–YSZ Substrates

Porous NiO–YSZ substrates with a thickness of 250 μm and a surface area of $10 \times 10 \text{ cm}^2$ were manufactured by SolydEra company, which are used as anode support for state-of-the-art planar SOFCs. The processing of the substrates was optimized for the maximization of performance and stability, using commercially viable manufacturing techniques. Thus, NiO–YSZ composite was manufactured by tape-casting using water suspensions and sintered at $\sim 1400 \text{ }^\circ\text{C}$ [55,56]. Further experimental details can be found in previous works. Afterward, NiO–YSZ plates were cut to obtain specimens of $20 \times 20 \text{ mm}^2$. The surfaces of the plates were ground with 600-, 800- and 1200-grit SiC papers, and polished using 30 μm and 3 μm diamond suspensions (Norton). The density of NiO–YSZ substrates at the surface was determined using the free, open-source software, ImageJ.

2.2. Laser Machining Treatment

A solid-state Nd:YLF Q-switched laser set-up (Spectra-Physics Explorer One 349–120) was employed to machine linear tracks on the NiO–YSZ surfaces. The laser is capable of emitting laser beams at 349 nm wavelength and a pulse width of up to 5 ns. The maximum output characteristics of the laser are a nominal output power of 60 W, a beam type TEM₀₀, and a quality factor $M^2 < 1.3$. As shown in Figure 1, the set-up was equipped with a platform consisting of a 2-axis laser beam deflection unit that controls the movement of the focus point on the XY-plane, together with two mirrors that adjust the trajectory of the laser beams. The sample is fixed on the sample holder, which is equipped with Vernier calipers along the x-, y- and z-axis. In this work, the laser beam was incident on the target surface at a 90-degree angle, a spot size diameter of 30 μm , and a scan rate of 6.0 mm/s. Preliminary work was focused on analyzing the influence of laser machining parameters—mainly the beam laser energy density (2.9–5.1 J/cm²) and the frequency (0.4–2.0 kHz)—on the surface quality and geometry of the track. For this purpose, laser patterns consisting of parallel tracks with a pitch of 100 μm between the parallel line tracks were chosen. Adequate laser-ablation conditions were selected combining complementarily optical and scanning electron microscopy inspection of all the machined tracks, maximizing a good balance between the track height, and the surface quality. For the next experiments, of the selected tracks, the line pitch between the parallel tracks was adjusted to the dimensions of the track-like features.

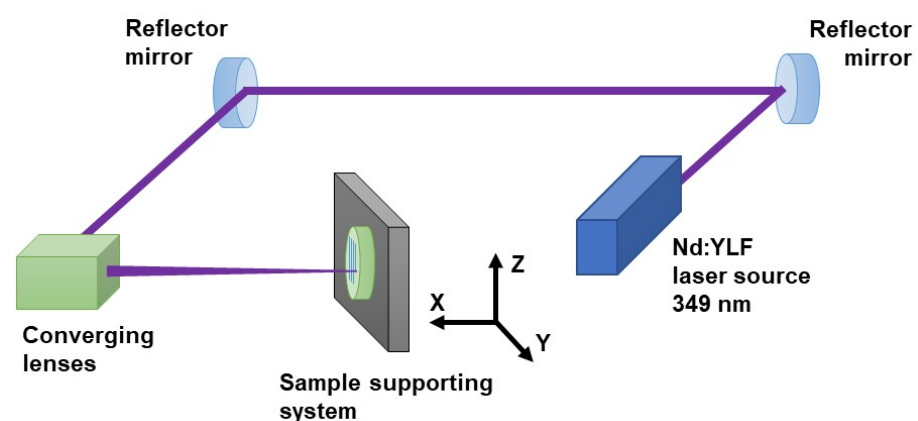


Figure 1. Sketch of laser equipment and optical composing the experimental setup at our laboratory.

2.3. Characterization Techniques

Since laser machining may induce irreversible changes, special attention was paid to evaluating possible damage induced at the surface of the machined tracks. The surface integrity evaluation was conducted through complementary analytical, microstructural and mechanical techniques.

2.3.1. Surface Topography

The topography of the laser-machined surfaces was characterized using a Contact Profilometer (Dektak 150 Stylus, Bruker, Billerica, MA, USA). A tip with a radius of 50 nm was employed at a force of 5 mg for scanning a total length of 400 μm . Confocal Laser Optical Profilometer (Olympus Lext OLS30, Tokio, Japan) equipped with several lens objectives from $\times 10$ to $\times 100$ was employed to determine the surface roughness of the local regions in the laser tracks. The surface roughness parameter (R_a) of blank, pile-up and valley regions for samples was determined, using the profilometer software, from the average of 5 measurements with a cut-off length of 128 μm .

2.3.2. Scanning Electron Microscopy (SEM)

The microstructure of machined samples was carried out employing a field emission scanning electron microscope (Carl Zeiss Merlin FESEM, Oberkochen, Germany) equipped with Energy Dispersive Spectroscopy (EDS) (Oxford Instruments INCA-350 system, United Kingdom). Samples were coated with carbon to minimize the electrical charge of the surface. Image analysis was performed on the top and cross-section surfaces of the laser tracks. Focused Ion Beam (FIB, Carl Zeiss Neon 40, Oberkochen, Germany) was used to prepare the cross-sections to observe the microstructure of the material, below the machined surface, with FESEM.

2.3.3. X-ray Diffraction (XRD)

The study of the crystalline phases was performed via X-ray diffraction (XRD, Bruker, D8-Advance, Karlsruhe, Germany) using $\text{Cu K}\alpha$ radiation (40 kV and 40 mA). Phase identification was carried out using the JCPDS database and the DIFFRACplus EVA software by Bruker AXS.

2.3.4. Raman Spectroscopy

The location of secondary phases was determined using Raman spectroscopy (inVia Qontor, Renishaw) at a wavelength of 532 nm as the applied excitation line, and $100\times$ objective in an optical microscope was employed.

2.3.5. X-ray Photoelectron Spectroscopy (XPS)

The chemical composition at the surface was determined with X-ray Photoelectron Spectroscopy (XPS) with a SPECS system (Surface Nano Analysis GmbH) equipped with an Al anode XR50 source operating at 150 W and a PHOIBOS 150 EP hemispherical energy analyzer with MCD-9 detector. The fitting and peak integration of spectra was carried out using Casa XPS software. The binding energies were calibrated to the C 1s peak (284.6 eV) to compensate for any charging effects.

2.3.6. Nanoindentation Tests

The mechanical properties of laser-machined surfaces were determined with the instrumented indentation technique. Tests were performed using an MTS Nanoindenter XP with a continuous stiffness measurement module. A Berkovich diamond tip was employed, which was calibrated with a fused silica standard. Experimental data were analyzed with the Oliver and Pharr method [57]. The laser-machined samples were encapsulated in a resin (Buehler, Lake Bluff, IL, USA) before the polishing and laser machining processes. In this case, the surfaces were ground with 600-, 800-, and 1200-grit SiC papers, polished using 30 μm and 3 μm diamond suspensions, and the last step with colloidal silica. Tests were

carried out on the top surface of the valley and pile-up tracks, and the untreated surface. For each region explored, two arrays of 25 imprints (5×5) were performed at 2000 nm of maximum displacement into the surface. A constant distance of 50 μm between contiguous imprints was held to prevent the overlapping effect between imprints and to ensure the test at the center of the laser track.

3. Results and Discussion

3.1. Surface Topography

Figure 2a shows the schematic definition of the height and width for a laser track, and the effect of laser parameters (energy density and frequency) on the surface topography. Figure 2b,c exhibit the surface topography as a function of the energy density at 1.0 kHz, and varying the laser frequency at 4.3 J/cm^2 , respectively. Additionally, Figures 3 and 4 illustrate the 3D images of surface topography as a function of the energy density and the laser frequency, respectively. Table 1 summarizes the dimension values of valley and pile-up for each laser condition. Increasing the energy density from 2.9 to 5.1 J/cm^2 at 1.0 kHz, H_t and W_t were increased from 0.87 μm to 3.38 μm , and from 18.5 μm to 37.1 μm , respectively. On the other side, frequencies between 0.4 kHz and 2.0 kHz at 4.3 J/cm^2 generated tracks of 0.91–2.08 μm H_t and 20.8–35.1 μm W_t . For the explored conditions, the pile-up induced with the laser track contributed between 24% and 29% of the total track depth. The width attributed to the sum of the two pile-ups (W_p) was between 39% and 48% of the total track width (W_t). The pile-up may enlarge the contact surface between the electrode and electrolyte. However, the pile-up is generated with molten and evaporated material as well as splashes of redeposited material from the laser track. Therefore, its microstructure and chemical composition could be quite different compared to the unmachined material, decreasing the electrochemical and mechanical performance of the cell. The extension of material pile-up mainly depends on the accuracy of the laser. Compared with pico- or femtosecond lasers, the accuracy of our laser is much lower, which also generates a wider laser track [58].

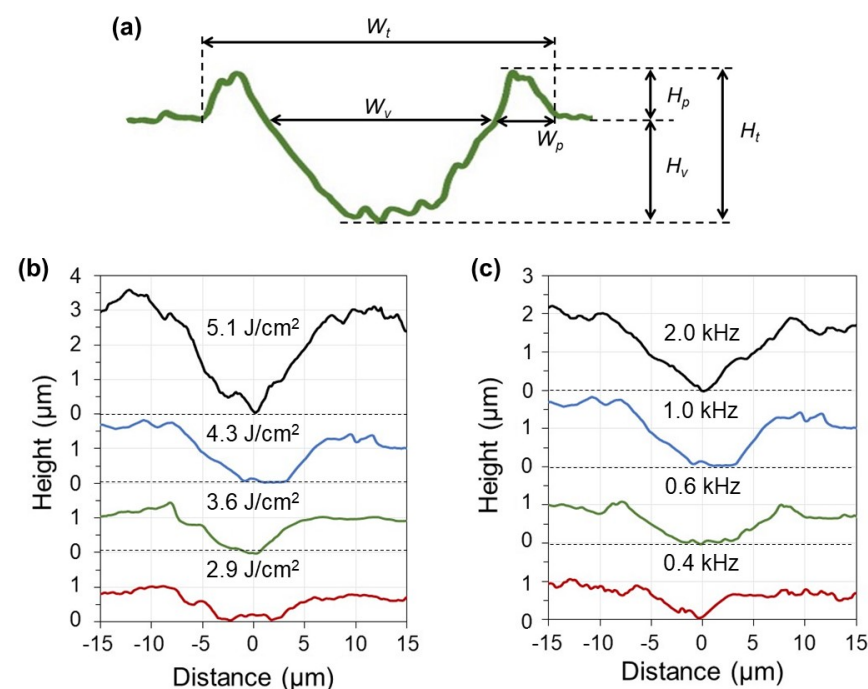


Figure 2. (a) Scheme of the profile for a laser track on a sample, indicating that H_v corresponds to the height valley; H_p , the pile-up height; H_t , the total height of track; W_v , the laser width; W_p , the pile-up width; and W_t , the total width of track. Topographic profiles of the laser tracks, recorded perpendicularly to the laser trench, varying: (b) the laser beam energy density at 1.0 kHz, and (c) the frequency at 4.3 J/cm^2 .

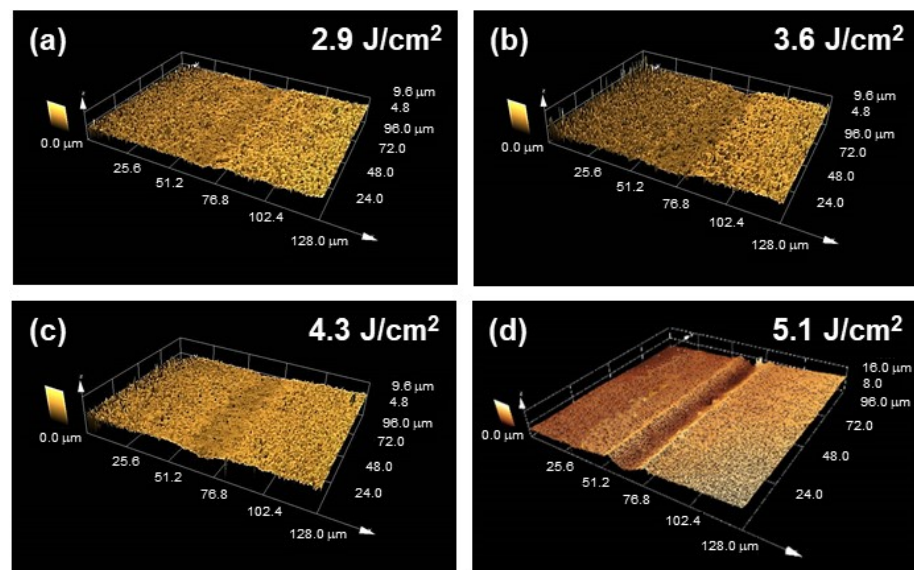


Figure 3. Topographic profiles for laser machined surfaces obtained at 1.0 kHz frequency and a laser energy density of: (a) 2.9 J/cm², (b) 3.6 J/cm², (c) 4.3 J/cm², and (d) 5.1 J/cm².

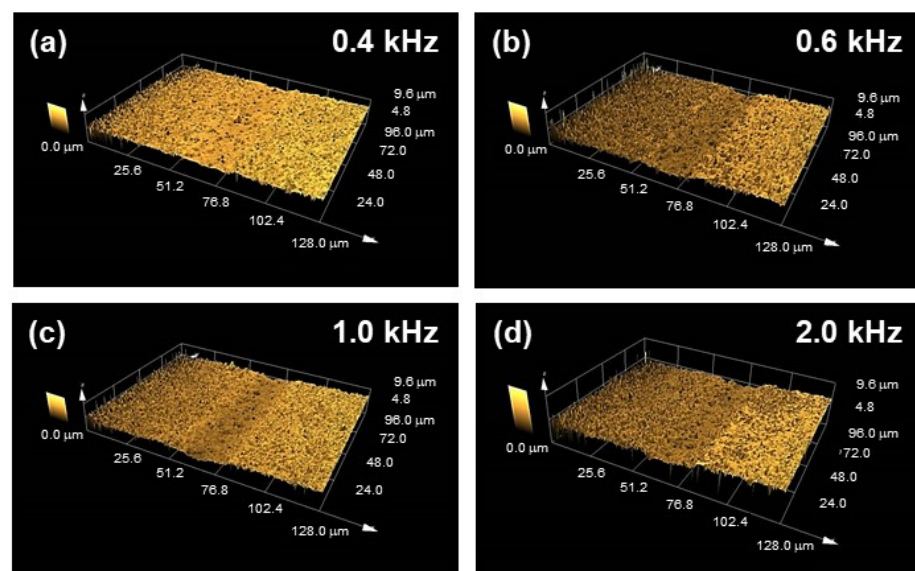


Figure 4. Topographic profiles for laser machined surfaces obtained at a laser energy density of 4.3 J/cm² and a frequency of: (a) 0.4 kHz, (b) 0.6 kHz, (c) 1.0 kHz, and (d) 2.0 kHz.

Table 1. Values of H_v the height valley; H_p , the pile-up height; H_t , the total height of track; W_v , the laser width; W_p , the pile-up width; and W_t , the total width of track for each energy density and frequency of the laser machined surfaces.

Energy Density (J/cm ²)	Frequency (kHz)	H_v (μm)	H_p (μm)	H_t (μm)	W_v (μm)	W_p (μm)	W_t (μm)
2.9	1.0	0.72 ± 0.07	0.27 ± 0.08	0.91 ± 0.12	13.2 ± 0.5	4.1 ± 0.3	20.8 ± 1.2
4.3	0.4	0.67 ± 0.07	0.23 ± 0.07	0.87 ± 0.14	11.5 ± 0.4	3.8 ± 0.3	18.5 ± 1.1
4.3	0.6	0.81 ± 0.09	0.36 ± 0.08	1.05 ± 0.15	15.3 ± 0.7	4.4 ± 0.2	24.1 ± 1.2
3.6	1.0	1.12 ± 0.11	0.41 ± 0.10	1.31 ± 0.18	15.1 ± 0.8	5.8 ± 0.8	26.7 ± 2.2
4.3	1.0	1.48 ± 0.13	0.45 ± 0.11	1.86 ± 0.21	16.4 ± 0.9	6.1 ± 0.9	28.6 ± 2.6
4.3	2.0	1.71 ± 0.18	0.59 ± 0.12	2.08 ± 0.28	18.7 ± 0.8	8.2 ± 1.1	35.1 ± 2.8
5.1	1.0	2.82 ± 0.26	0.86 ± 0.13	3.38 ± 0.38	19.3 ± 0.9	8.9 ± 1.2	37.1 ± 2.7

On the other hand, laser machining produces splashes of redeposited material and cracks, which generates significant roughness along the valley and pile-up surfaces. Therefore, the roughness of the laser trench is an interesting parameter to evaluate the surface quality. Table 2 shows the roughness (R_a) determined parallel to the laser track. R_a values between 0.14 and 0.31 μm in the valley surfaces were obtained. R_a obtained for pile-up was close to that of the valley, however, these values are in the same order as the height of the pile-up, and therefore, this roughness does not seem controllable. The roughness results at the valley were larger than those of a polished surface ($R_a < 0.1 \mu\text{m}$). Therefore, the laser machining generated a roughness on the polished surface much lower than the tape-casted NiO–YSZ composite ($R_a > 1 \mu\text{m}$). Furthermore, the presence of this roughness may enhance the electrode and electrolyte adhesion.

Table 2. Values of surface roughness (R_a) at the laser machined surfaces recorded parallel to the laser trench in the valley region.

Energy Density (J/cm^2)	Frequency (kHz)	R_a at Valley (μm)
2.9	1.0	0.16 ± 0.03
4.3	0.4	0.14 ± 0.03
4.3	0.6	0.15 ± 0.02
3.6	1.0	0.17 ± 0.02
4.3	1.0	0.18 ± 0.03
4.3	2.0	0.28 ± 0.08
5.1	1.0	0.31 ± 0.09

The specific goal of this work was to reproduce laser tracks within the typical range of energy density (3.3–6.4 J/cm^2) [31,49,58] for SOFC materials with good surface quality to analyze the damage and possible microstructure changes. Accordingly, laser parameters selected for the processing of laser tracks were at 4.3 J/cm^2 and 1.0 kHz, thus obtaining a valley depth close to 2 μm with a roughness lower than 0.20 μm and a minimized pile-up size. This laser track presented a valley depth smaller than that required for a remarkable modification of the electrode–electrolyte interface in an anode-supported SOFC, as the valley typically presents from a few to tens of micrometers [32–41,58]. Therefore, it is assumed that this laser track was satisfactory for subsequent studies related to microstructure and phase changes, and chemical and mechanical tests. Concerning the laser patterns, two series of samples were prepared: one with the line pitch adjusted to 100 μm for SEM and Nanoindentation tests, and another with 20 μm for FIB-SEM, XRD, Raman and XPS analyses to increase the signal of possible effects due to the laser–material interaction.

3.2. Microstructure

Figure 5 shows the FESEM surface images of laser tracks fabricated at 4.3 J/cm^2 and 1.0 kHz, compared to a blank surface of NiO–YSZ. The valley region of the laser track presented microcracks and a surface microstructure denser than the blank one, which is attributed to the thermal effects of laser treatment. In addition, the microstructure of the pile-up region also exhibited a lower porosity than untreated NiO–YSZ (Figures 5 and 6). It is due to the material vaporization of the laser-track valley, which can be partly deposited, in nanoparticle form, on top of the pile-up surface and a region close to the valley region. The presence of the denser layer with larger NiO and YSZ mean grain size at the laser tracks could lead to undesirable effects, such as the loss of gas transport, electrical connectivity and mechanical reliability of the final product, which is a porous Ni–YSZ cermet. Therefore, it could affect the electrochemical and mechanical properties of Ni–YSZ anode in a real application. However, the reduction of the NiO–YSZ composite to Ni–YSZ cermet at the typical conditions (750 $^\circ\text{C}$ using from 5% H_2/Ar to 100% H_2) evidenced the change in this layer to form a Ni–YSZ microstructure with ~18% porosity (Figure 6).

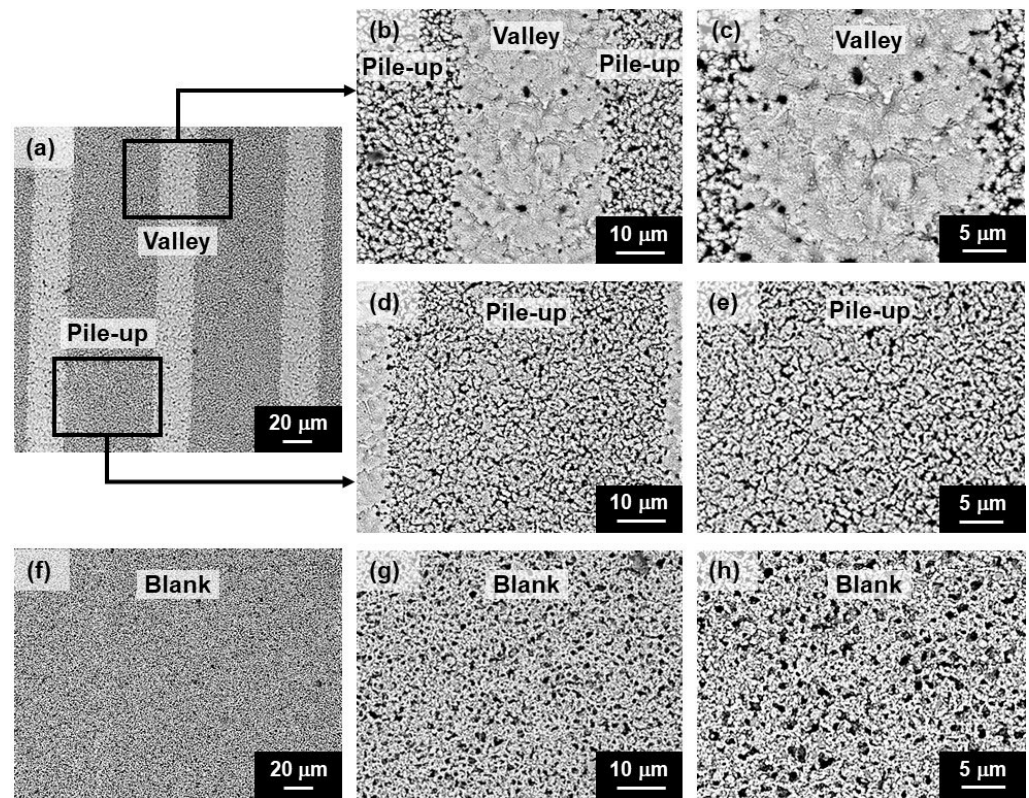


Figure 5. FESEM surface images of: (a) three laser tracks fabricated at 4.3 J/cm^2 and 1.0 kHz , (b,c) the valley region, and (d,e) the pile-up region; and (f–h) blank NiO–YSZ.

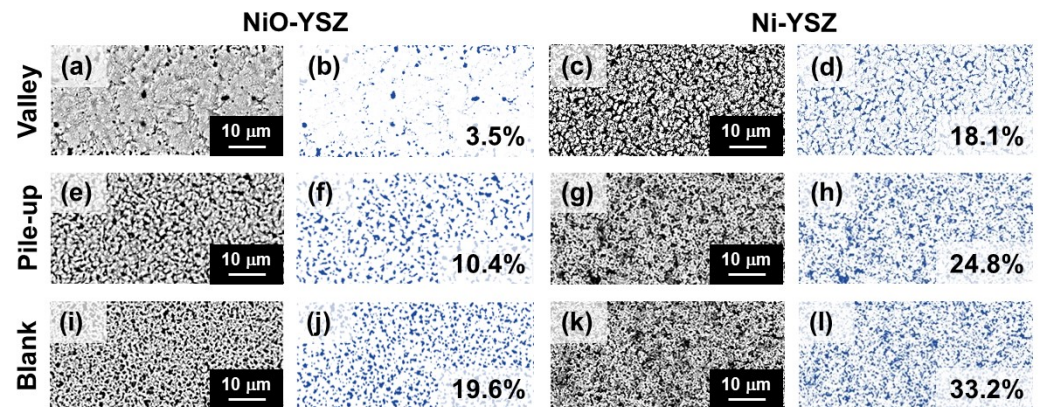


Figure 6. FESEM images of laser tracks fabricated at 4.3 J/cm^2 and 1.0 kHz , showing surface porosity (in highlighted in blue) corresponding to: (a–d) the valley region, and (e–h) the pile-up region; and (i–l) blank for NiO–YSZ and Ni–YSZ.

The extension of the HAZ was studied with the FIB-FESEM images of a cross-sectional laser track and blank NiO–YSZ (Figure 7). The HAZ affected a first layer of grains (around $2 \mu\text{m}$) below the machined surface, presenting recrystallization to equiaxial grains and decreasing the porosity in the vicinity of the machined areas (Figure 7a,b). In addition, intergranular micro-cracks were observed at the top-surface, which propagated perpendicularly to the surface (Figure 7a). This particular microstructure at the surface is typically generated due to the photothermal-mechanical process of the laser ablation, in which the material is essentially removed due to the thermal mechanisms activated through the laser radiation [42,43]. Below the recrystallized material, the microstructure of laser machined exhibited typical properties similar to the blank material (Figure 7b,c).

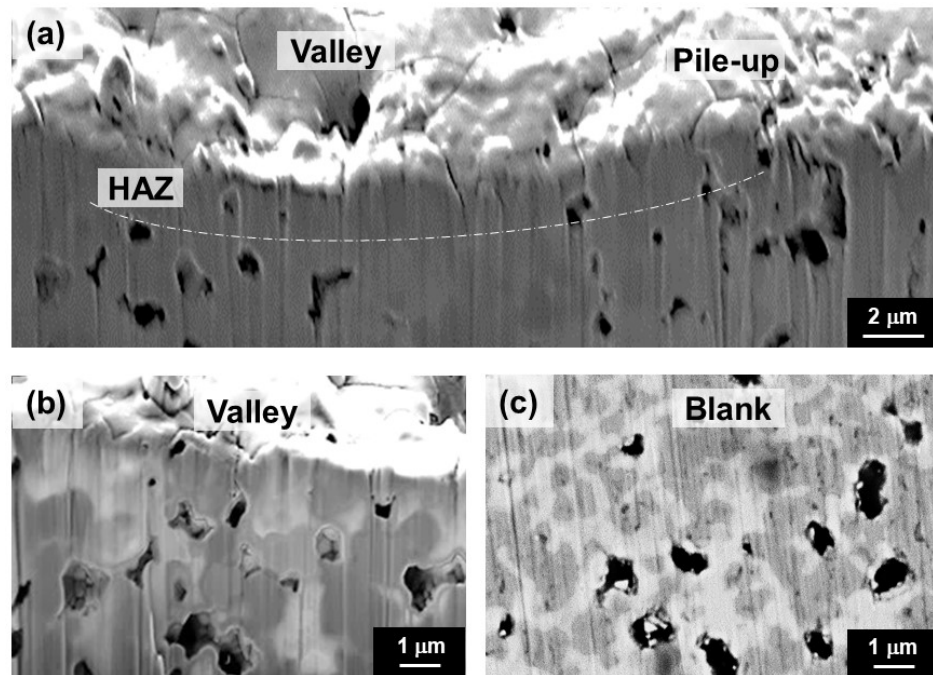


Figure 7. FIB-FESEM images of the cross-section corresponding to: (a,b) a laser machined surface at 4.3 J/cm^2 and 1.0 kHz , and (c) a blank surface (unmachined).

3.3. Crystalline Phases

The XRD spectra of the NiO–YSZ samples, before and after the laser machining process, are shown in Figure 8. Both samples presented tetragonal and two monoclinic peaks (at 28° and 31°) corresponding to YSZ. However, the monoclinic peaks were more intense in the machined sample, as these exhibited an intensity about four times higher than the blank sample (unmachined). In addition, the comparison of both XRD spectra evidenced that the most intense peak of NiO (at 43°) presented a decrease in intensity of around 6% for the machined sample. It may be mainly attributed to the major evaporation and ejection of NiO compared to YSZ during laser treatment, which is in good concordance with no presence of metallic Ni, in the position of the most intense peak at 45° , detected in the XRD of the machined sample.

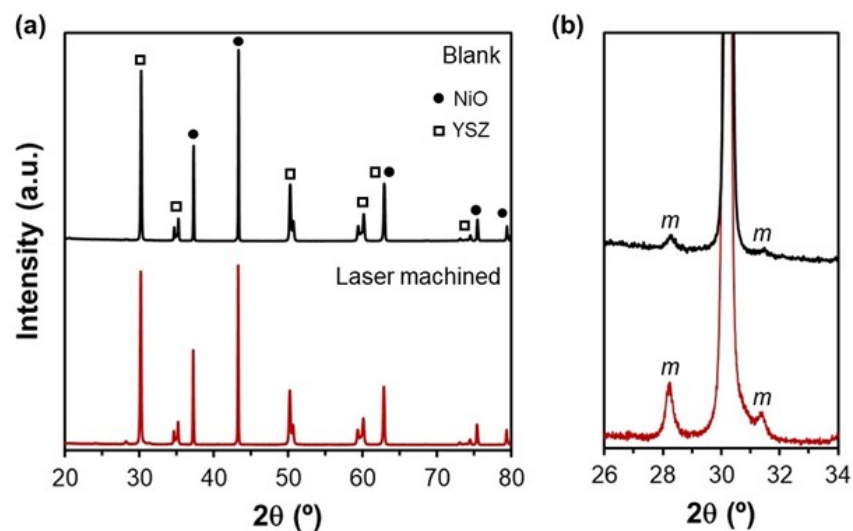


Figure 8. (a) XRD spectra of the blank and laser machined NiO–YSZ at 4.3 J/cm^2 and 1.0 kHz , and (b) zoom graph of XRD spectra within the $26\text{--}34^\circ$ region. Diffraction peaks of the monoclinic phase are indicated with “m”.

To assess the location of the monoclinic phase at zirconia transformed due to the thermal effect of laser treatment on the NiO–YSZ surface, FESEM and Raman spectroscopy were combined. Figure 9 shows a FESEM image at the valley of a laser track, and Raman spectra at different points near a crack generated during the laser treatment. When qualitatively observing the Raman spectra, the monoclinic phase is mainly located close to the crack. In contrast, the zones far away from the micro-crack (points 1 and 5) presented only a tetragonal phase. These results are in good agreement with our previous work of laser treatment on the YSZ surface, in which the tetragonal phase was mainly transformed to monoclinic in the regions close to cracks [54].

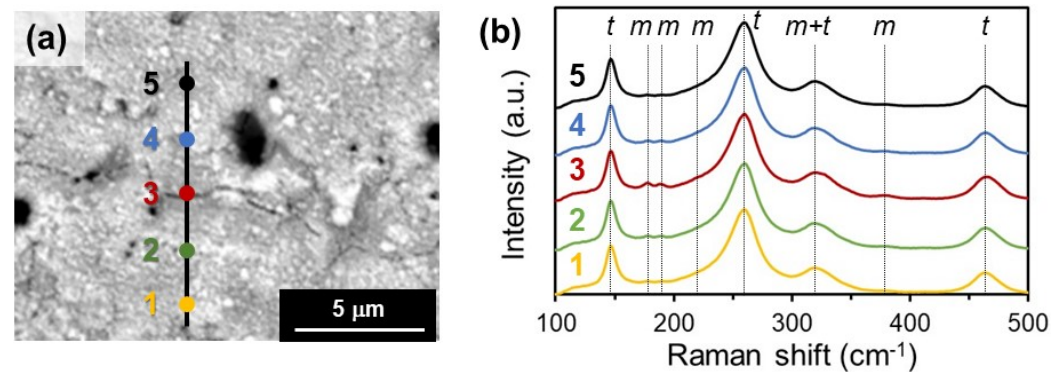


Figure 9. (a) FESEM image, and (b) Raman spectra of the laser machined surface at the points marked with numbers. Raman peaks of the monoclinic and tetragonal phases are indicated with “m” and “t”.

3.4. Chemical Composition

The XPS technique was employed to determine the changes in the elemental composition at the surface due to the laser-machining treatment. Figure 10 shows the XPS spectra of the main elements for the unmachined and laser-machined NiO–YSZ surfaces. In Figure 10a, the Zr 3d core-level spectrum, peaks corresponding to Zr 3d_{3/2} (at ~184.5 eV) and Zr 3d_{5/2} (at ~182 eV) indicated the presence of Zr–O bonds typically observed in ZrO₂ and YSZ [59,60]. Similarly, the Y 3d core-level spectrum consisted of two deconvoluted peaks at 157 and 159 eV, which correspond to Y 3d_{5/2} and Y 3d_{3/2} of Y–O bindings, respectively (Figure 10b). In terms of the Y₂O₃ dopant concentration, the estimated Y/Zr ratio after laser machining was close to the unmachined sample with a difference of less than 4%. In Figure 10c, the deconvolution of two peaks at 854 and 856 eV belong to Ni 2p_{3/2}, and the satellite peak at 861 eV, corresponded to nickel oxide with Ni²⁺ and Ni³⁺ states, respectively [61–63]. The laser-machined NiO–YSZ composite presented a slight decrease in Ni, which corresponded to a reduction of about 5% for the machined sample and was in good concordance with the XRD results. The O 1s spectrum was deconvoluted in three peaks at 529, 531 and 532 eV probably associated with metal–oxygen lattice, oxygen vacancy and chemisorbed oxygen species, respectively (Figure 10d) [64–66]. Thus, no significant elemental segregation was detected at the surface. Both the Ni content and the Y₂O₃ dopant concentration in YSZ were maintained, which is crucial for guaranteeing good electronic and ionic conductivity at the anode.

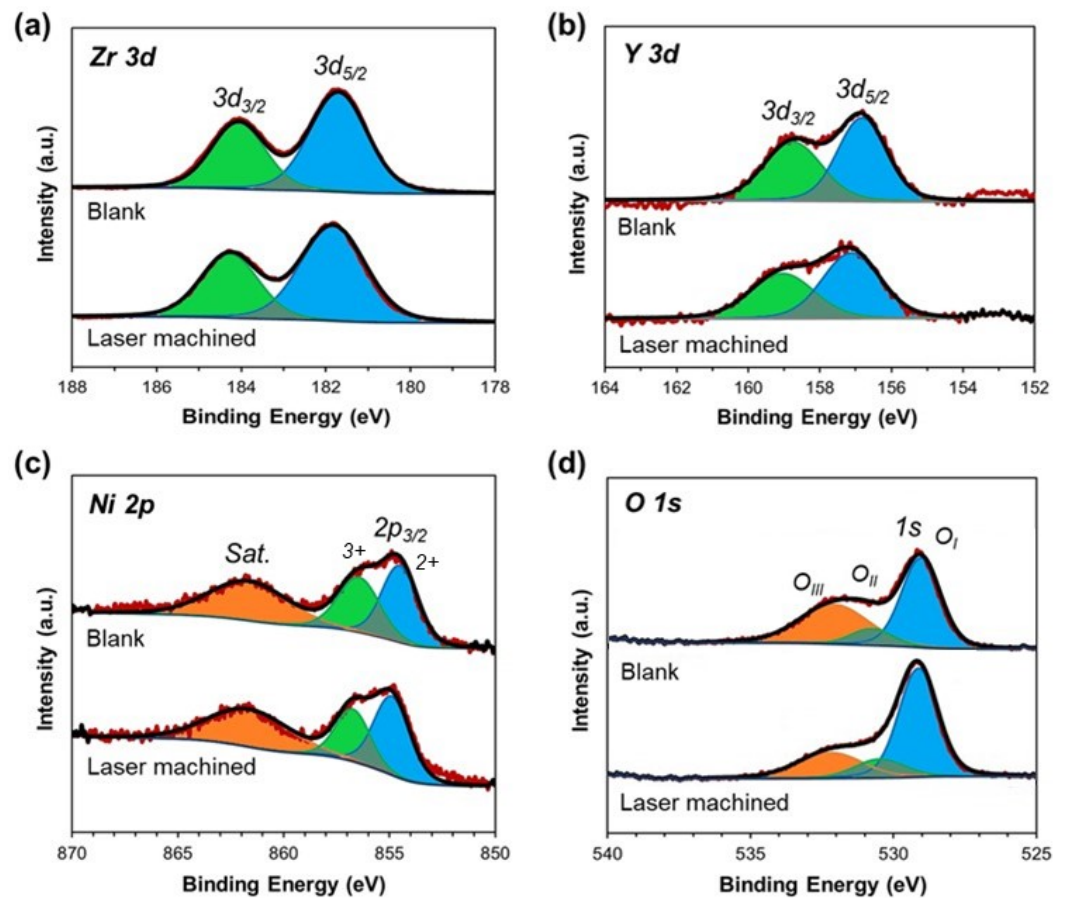


Figure 10. XPS spectra of: (a) Zr, (b) Y, (c) Ni, and (d) O, for the blank and laser-treated NiO-YSZ surfaces at 4.3 J/cm^2 and 1.0 kHz .

3.5. Mechanical Properties

The mechanical properties of laser-treated surfaces were studied using the instrumented Nanoindentation technique, assessing the evolution of Elastic Modulus (E) and Hardness (H) with the indenter indentation depth. Figure 11 shows the mechanical properties at the valley and the pile-up of laser-machined surfaces, which were compared to the blank surface. Both E and H of the blank surface and the pile-up surface gradually decreased with increasing indentation depth. This decrease in E and H was attributed to the internal defects, such as porosity and voids, present in the NiO-YSZ composite. In contrast, the mechanical properties at the valley of laser-treated surfaces presented a significant decrease at low indentation depths (within the range of 0–200 nm), which were recovered as the indenter penetrated further into the laser-machined surfaces. This drop at low indentation depths could be due to the presence of microcracks and certain roughness at the laser-treated surface, due to the thermal effects and the induced topography caused by laser treatment. Finally, the values of E and H determined for the laser-machined NiO-YSZ surfaces were close to those reported in previous works using the nanoindentation technique [67,68].

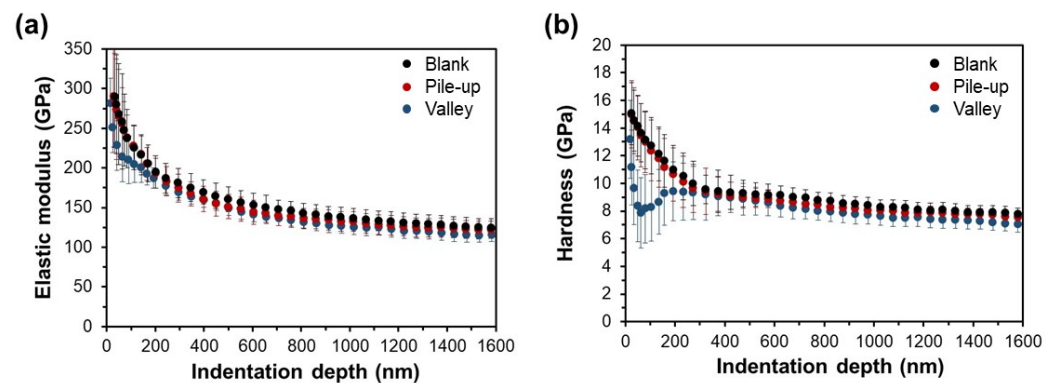


Figure 11. (a) Elastic Modulus and (b) Hardness as a function of the indentation depth, testing on the valley of the laser-track, pile-up (laser-tracked peripheral surface), and blank surface.

4. Conclusions

The surface topography of the state-of-the-art NiO–YSZ composites for SOFCs was modified using a pulsed laser to explore its thermal effects on microstructure and surface quality. The main conclusions are as follows:

- The laser machining generated up to 2 μm thick laser-affected region, which presented intergranular microcracks and recrystallization with equiaxial grains. The valley surface of laser tracks presented micro-cracks and a denser microstructure than the blank one, which was attributed to the thermal effects of laser machining. The microstructure of the pile-up region also exhibited a lower porosity than the blank surface, due to the partly deposited material from vaporization.
- XRD and XPS analyses evidenced a small decrease in Ni (<5%) in the machined sample, which was mainly due to the major evaporation and ejection of NiO compared to YSZ during laser treatment. In addition, laser machining induced the doped zirconia transformation from the tetragonal to monoclinic phase on the treated surface, which was limited to only the regions close to cracks.
- Nanoindentation tests showed that the laser-treated surfaces only presented a decrease in elastic modulus and hardness at low indentation depths (within the range of 0–200 nm). It was attributed to the presence of micro-cracks, and certain roughness at the laser-treated surface, due to the thermal effects and the induced topography caused by laser treatment. Therefore, this corroborated that the damage and the extension of HAZ induced during the laser treatment were very limited.

All in all, laser machining could be an interesting post-processing treatment for sintered NiO–YSZ composites, as the laser-affected region at the surface was local to the selected conditions. However, the microstructure changes should be evaluated to ensure the functionality, in terms of electrochemical performance, structural integrity and reliability, of the laser-machined NiO–YSZ composites used as anode precursors in SOFC applications.

Author Contributions: Conceptualization, M.M., M.P. and E.J.-P.; methodology, M.M., S.G.-G., M.P., D.M. and E.J.-P.; software, M.M. and M.P.; validation, M.M., S.G.-G. and M.P.; formal analysis, M.M., M.P., D.M. and E.J.-P.; investigation, M.M., S.G.-G., M.P. and E.J.-P.; resources, M.M., D.M. and E.J.-P.; data curation, M.M. and M.P.; writing—original draft preparation, M.M.; writing—review and editing, M.M., S.G.-G., M.P., D.M. and E.J.-P.; visualization, M.M. and M.P.; supervision, M.M., S.G.-G., M.P., D.M. and E.J.-P.; project administration, M.M., D.M. and E.J.-P.; funding acquisition, M.M. and E.J.-P. All authors have read and agreed to the published version of the manuscript.

Funding: This research has been supported by grant PID2021-126614OB-I00, funded by MCIN/AEI/10.13039/501100011033, and AGAUR, Agency for Administration of University and Research (Agència de Gestió d'Ajuts Universitaris i de Recerca) (2021 SGR 01053). Miguel Morales Comas is Serra Húnter Lecturer Professor and he is grateful to Serra Húnter program (Generalitat de Catalunya).

Conflicts of Interest: The authors declare no conflict of interest.

References

1. Stambouli, A.B.; Traversa, E. Solid Oxide Fuel Cells (SOFCs): A Review of an Environmentally Clean and Efficient Source of Energy. *Renew. Sustain. Energy Rev.* **2002**, *6*, 433–455. [\[CrossRef\]](#)
2. Singhal, S.C.; Kendall, K. *High-Temperature Solid Oxide Fuel Cells: Fundamentals, Design, and Applications*; Elsevier: Amsterdam, The Netherlands, 2003; p. 405.
3. Zakaria, Z.; Abu Hassan, S.H.; Shaari, N.; Yahaya, A.Z.; Boon Kar, Y. A Review on Recent Status and Challenges of Yttria Stabilized Zirconia Modification to Lowering the Temperature of Solid Oxide Fuel Cells Operation. *Int. J. Energy Res.* **2020**, *44*, 631–650. [\[CrossRef\]](#)
4. Hussain, S.; Yangping, L. Review of Solid Oxide Fuel Cell Materials: Cathode, Anode, and Electrolyte. *Energy Transit.* **2020**, *4*, 113–126. [\[CrossRef\]](#)
5. Mahato, N.; Banerjee, A.; Gupta, A.; Omar, S.; Balani, K. Progress in Material Selection for Solid Oxide Fuel Cell Technology: A Review. *Prog. Mater. Sci.* **2015**, *72*, 141–337. [\[CrossRef\]](#)
6. Lee, J.H.; Moon, H.; Lee, H.W.; Kim, J.; Kim, J.D.; Yoon, K.H. Quantitative Analysis of Microstructure and Its Related Electrical Property of SOFC Anode, Ni–YSZ Cermet. *Solid State Ionics* **2002**, *148*, 15–26. [\[CrossRef\]](#)
7. Morales, M.; Laguna-Bercero, M.Á. Influence of Anode Functional Layers on Electrochemical Performance and Mechanical Strength in Microtubular Solid Oxide Fuel Cells Fabricated by Gel-Casting. *ACS Appl. Energy Mater.* **2018**, *1*, 2024–2031. [\[CrossRef\]](#)
8. Brus, G.; Miyawaki, K.; Iwai, H.; Saito, M.; Yoshida, H. Tortuosity of an SOFC Anode Estimated from Saturation Currents and a Mass Transport Model in Comparison with a Real Micro-Structure. *Solid State Ionics* **2014**, *265*, 13–21. [\[CrossRef\]](#)
9. Morales, M.; Laguna-Bercero, M.A.; Navarro, M.E.; Espiell, F.; Segarra, M. The Effect of Anode Support on the Electrochemical Performance of Microtubular Solid Oxide Fuel Cells Fabricated by Gel-Casting. *RSC Adv.* **2015**, *5*, 39350–39357. [\[CrossRef\]](#)
10. Tjaden, B.; Brett, D.J.L.; Shearing, P.R. Tortuosity in Electrochemical Devices: A Review of Calculation Approaches. *Int. Mater. Rev.* **2016**, *63*, 47–67. [\[CrossRef\]](#)
11. Smith, J.R.; Chen, A.; Gostovic, D.; Hickey, D.; Kundinger, D.; Duncan, K.L.; DeHoff, R.T.; Jones, K.S.; Wachsman, E.D. Evaluation of the Relationship between Cathode Microstructure and Electrochemical Behavior for SOFCs. *Solid State Ionics* **2009**, *180*, 90–98. [\[CrossRef\]](#)
12. Bertei, A.; Ruiz-Trejo, E.; Kareh, K.; Yufit, V.; Wang, X.; Tariq, F.; Brandon, N.P. The Fractal Nature of the Three-Phase Boundary: A Heuristic Approach to the Degradation of Nanostructured Solid Oxide Fuel Cell Anodes. *Nano Energy* **2017**, *38*, 526–536. [\[CrossRef\]](#)
13. Morales, M.; Laguna-Bercero, M.A. Microtubular Solid Oxide Fuel Cells Fabricated by Gel-Casting: The Role of Supporting Microstructure on the Mechanical Properties. *RSC Adv.* **2017**, *7*, 17620–17628. [\[CrossRef\]](#)
14. Su, H.; Hu, Y.H. Progress in Low-Temperature Solid Oxide Fuel Cells with Hydrocarbon Fuels. *Chem. Eng. J.* **2020**, *402*, 126235. [\[CrossRef\]](#)
15. Bernadet, L.; Morales, M.; Capdevila, X.G.; Ramos, F.; Monterde, M.C.; Calero, J.A.; Morata, A.; Torrell, M.; Tarancón, A. Reversible Fuel Electrode Supported Solid Oxide Cells Fabricated by Aqueous Multilayered Tape Casting. *J. Phys. Energy* **2021**, *3*, 024002. [\[CrossRef\]](#)
16. Morales, M.; Laguna-Bercero, M.A.; Jiménez-Piqué, E. Direct-Methane Anode-Supported Solid Oxide Fuel Cells Fabricated by Aqueous Gel-Casting. *J. Eur. Ceram. Soc.* **2023**, *43*, 2740–2751. [\[CrossRef\]](#)
17. He, S.; Jiang, S.P. Electrode/Electrolyte Interface and Interface Reactions of Solid Oxide Cells: Recent Development and Advances. *Prog. Nat. Sci. Mater. Int.* **2021**, *31*, 341–372. [\[CrossRef\]](#)
18. Tsumori, F.; Xu, Y.; Tanaka, Y.; Osada, T.; Miura, H. Micrometer-Scale Imprinting Process for Ceramic Sheet from Powder Compound Material. *Procedia Eng.* **2014**, *81*, 1433–1438. [\[CrossRef\]](#)
19. Dai, H.; He, S.; Chen, H.; Guo, L. A Novel Method of Modifying Electrolyte Surface at Mesoscale for Intermediate-Temperature Solid Oxide Fuel Cells. *Ceram. Int.* **2016**, *42*, 2045–2050. [\[CrossRef\]](#)
20. Timurkutluk, C.; Altan, T.; Yildirim, F.; Onbilgin, S.; Yagiz, M.; Timurkutluk, B. Improving the Electrochemical Performance of Solid Oxide Fuel Cells by Surface Patterning of the Electrolyte. *J. Power Sources* **2021**, *512*, 230489. [\[CrossRef\]](#)
21. Timurkutluk, C.; Altan, T.; Onbilgin, S.; Yildirim, F.; Yagiz, M.; Timurkutluk, B. Mesh Patterned Electrolyte Supports for High-Performance Solid Oxide Fuel Cells. *Int. J. Energy Res.* **2022**, *46*, 10689–10703. [\[CrossRef\]](#)
22. Gao, M.; Li, C.X.; De Wang, M.; Wang, H.L.; Li, C.J. Influence of the Surface Roughness of Plasma-Sprayed YSZ on LSM Cathode Polarization in Solid Oxide Fuel Cells. *Key Eng. Mater.* **2008**, *373–374*, 641–644. [\[CrossRef\]](#)
23. Wang, X.M.; Li, C.X.; Huang, J.Y.; Yang, G.J.; Li, C.J. Deposition Mechanism of Convex YSZ Particles and Effect of Electrolyte/Cathode Interface Structure on Cathode Performance of Solid Oxide Fuel Cell. *Int. J. Hydrogen Energy* **2014**, *39*, 13650–13657. [\[CrossRef\]](#)
24. Xu, Y.; Tsumori, F.; Osada, T.; Miura, H. Improvement of Solid Oxide Fuel Cell by Imprinted Micropatterns on Electrolyte. *Micro Nano Lett.* **2013**, *8*, 571–574. [\[CrossRef\]](#)
25. Farandos, N.M.; Kleiminger, L.; Li, T.; Hankin, A.; Kelsall, G.H. Three-Dimensional Inkjet Printed Solid Oxide Electrochemical Reactors. I. Yttria-Stabilized Zirconia Electrolyte. *Electrochim. Acta* **2016**, *213*, 324–331. [\[CrossRef\]](#)
26. Salari, F.; Badihi Najafabadi, A.; Ghatee, M.; Golmohammad, M. Hybrid Additive Manufacturing of the Modified Electrolyte-Electrode Surface of Planar Solid Oxide Fuel Cells. *Int. J. Appl. Ceram. Technol.* **2020**, *17*, 1554–1561. [\[CrossRef\]](#)

27. Okabe, T.; Kim, Y.; Jiao, Z.; Shikazono, N.; Taniguchi, J. Fabrication Process for Micropatterned Ceramics via UV-Nanoimprint Lithography Using UV-Curable Binder. *Jpn. J. Appl. Phys.* **2018**, *57*, 106501. [[CrossRef](#)]
28. Akama, R.; Okabe, T.; Sato, K.; Inaba, Y.; Shikazono, N.; Sciazko, A.; Taniguchi, J. Fabrication of a Micropatterned Composite Electrode for Solid Oxide Fuel Cells via Ultraviolet Nanoimprint Lithography. *Microelectron. Eng.* **2020**, *225*, 111277. [[CrossRef](#)]
29. Masciandaro, S.; Torrell, M.; Leone, P.; Tarancón, A. Three-Dimensional Printed Yttria-Stabilized Zirconia Self-Supported Electrolytes for Solid Oxide Fuel Cell Applications. *J. Eur. Ceram. Soc.* **2019**, *39*, 9–16. [[CrossRef](#)]
30. Pesce, A.; Hornés, A.; Núñez, M.; Morata, A.; Torrell, M.; Tarancón, A. 3D Printing the next Generation of Enhanced Solid Oxide Fuel and Electrolysis Cells. *J. Mater. Chem. A* **2020**, *8*, 16926–16932. [[CrossRef](#)]
31. Merino, R.I.; Laguna-Bercero, M.A.; Lahoz, R.; Larrea, Á.; Oliete, P.B.; Orera, A.; Peña, J.I.; Sanjuán, M.L.; Sola, D. Laser Processing of Ceramic Materials for Electrochemical and High Temperature Energy Applications. *Boletín Soc. Española Cerámica Vidr.* **2021**, *61*, S19–S39. [[CrossRef](#)]
32. Cebollero, J.A.; Lahoz, R.; Laguna-Bercero, M.A.; Larrea, A. Tailoring the Electrode-Electrolyte Interface of Solid Oxide Fuel Cells (SOFC) by Laser Micro-Patterning to Improve Their Electrochemical Performance. *J. Power Sources* **2017**, *360*, 336–344. [[CrossRef](#)]
33. Cebollero, J.A.; Laguna-Bercero, M.A.; Lahoz, R.; Silva, J.; Moreno, R.; Larrea, A. Optimization of Laser-Patterned YSZ-LSM Composite Cathode-Electrolyte Interfaces for Solid Oxide Fuel Cells. *J. Eur. Ceram. Soc.* **2019**, *39*, 3466–3474. [[CrossRef](#)]
34. Cebollero, J.A.; Lahoz, R.; Laguna-Bercero, M.A.; Peña, J.I.; Larrea, A.; Orera, V.M. Characterization of Laser-Processed Thin Ceramic Membranes for Electrolyte-Supported Solid Oxide Fuel Cells. *Int. J. Hydrogen Energy* **2017**, *42*, 13939–13948. [[CrossRef](#)]
35. Cai, G.; Zhang, Y.; Dai, H.; He, S.; Ge, L.; Chen, H.; Guo, L. Modification of Electrode/Electrolyte Interface by Laser Micro-Processing for Solid Oxide Fuel Cell. *Mater. Lett.* **2017**, *195*, 232–235. [[CrossRef](#)]
36. Konno, A.; Iwai, H.; Saito, M.; Yoshida, H. A Corrugated Mesoscale Structure on Electrode–Electrolyte Interface for Enhancing Cell Performance in Anode-Supported SOFC. *J. Power Sources* **2011**, *196*, 7442–7449. [[CrossRef](#)]
37. Seo, H.; Kishimoto, M.; Nakagawa, T.; Iwai, H.; Yoshida, H. Mechanism of Improved Electrochemical Performance of Anode-Supported Solid Oxide Fuel Cells by Mesoscale Modification of Electrode–Electrolyte Interface. *J. Power Sources* **2021**, *506*, 230107. [[CrossRef](#)]
38. Liu, P.; Fan, S.; Liu, Y.; Han, X.; Jin, Z. Three-Dimensional Modeling of Anode-Supported Planar SOFC with Corrugated Electrolyte. *J. Electrochem. Soc.* **2021**, *168*, 104501. [[CrossRef](#)]
39. Zhang, Y.; Cai, G.; Gu, Y.; Ge, L.; Zheng, Y.; Chen, H.; Guo, L. Modifying the Electrode-Electrolyte Interface of Anode Supported Solid Oxide Fuel Cells (SOFCs) by Laser-Machining. *Energy Convers. Manag.* **2018**, *171*, 1030–1037. [[CrossRef](#)]
40. Gurauskis, J.; Sola, D.; Peña, J.I.; Orera, V.M. Laser Drilling of Ni–YSZ Cermets. *J. Eur. Ceram. Soc.* **2008**, *28*, 2673–2680. [[CrossRef](#)]
41. Gu, D.; Shi, N.; Yu, F.; Zheng, Y.; Chen, H.; Guo, L. Asymmetric Anode Substrate Fabricated by Phase Inversion Process and Its Interface Modification for Solid Oxide Fuel Cells. *J. Alloys Compd.* **2018**, *742*, 20–28. [[CrossRef](#)]
42. Samant, A.N.; Dahotre, N.B. Laser Machining of Structural Ceramics—A Review. *J. Eur. Ceram. Soc.* **2009**, *29*, 969–993. [[CrossRef](#)]
43. Gautam, G.D.; Pandey, A.K. Pulsed Nd:YAG Laser Beam Drilling: A Review. *Opt. Laser Technol.* **2018**, *100*, 183–215. [[CrossRef](#)]
44. Liang, L.; Yuan, J.; Lin, G. Effect of the Scanning Speed on the Microgroove Formation Regime in Nanosecond-Pulsed Laser Scanning Ablation of Cermet. *Int. J. Adv. Manuf. Technol.* **2020**, *107*, 97–107. [[CrossRef](#)]
45. Tsibidis, G.D.; Mansour, D.; Stratakis, E. Damage Threshold Evaluation of Thin Metallic Films Exposed to Femtosecond Laser Pulses: The Role of Material Thickness. *Opt. Laser Technol.* **2022**, *156*, 108484. [[CrossRef](#)]
46. Mutlu, M.; Kacar, E.; Akman, E.; Akkan, C.K.; Demir, P.; Demir, A. Effects of The Laser Wavelength on Drilling Process of Ceramic Using Nd:YAG Laser. *JLMN J. Laser Micro/Nanoeng.* **2009**, *4*, 84–88. [[CrossRef](#)]
47. Hejjaji, A.; Singh, D.; Kubher, S.; Kalyanasundaram, D.; Gururaja, S. Machining damage in FRPs: Laser versus conventional drilling. *Compos. A: Appl. Sci. Manuf.* **2016**, *82*, 42–52. [[CrossRef](#)]
48. Solati, A.; Hamed, M.; Safarabadi, M. Comprehensive Investigation of Surface Quality and Mechanical Properties in CO₂ Laser Drilling of GFRP Composites. *Int. J. Adv. Manuf. Technol.* **2019**, *102*, 791–808. [[CrossRef](#)]
49. Sola, D.; Gurauskis, J.; Peña, J.I.; Orera, V.M. Cold Laser Machining of Nickel-Yttrium Stabilised Zirconia Cermets: Composition Dependence. *Mater. Res. Bull.* **2009**, *44*, 1910–1915. [[CrossRef](#)]
50. Malbakhova, I.; Bagishev, A.; Vorobyev, A.; Borisenko, T.; Logutenko, O.; Titkov, A. Fabrication of NiO/YSZ-Based Anodes for Solid Oxide Fuel Cells by Hybrid 3D Inkjet Printing and Laser Treatment. *Ceramics* **2022**, *5*, 1115–1127. [[CrossRef](#)]
51. Roitero, E.; Lasserre, F.; Anglada, M.; Mücklich, F.; Jiménez-Piqué, E. A Parametric Study of Laser Interference Surface Patterning of Dental Zirconia: Effects of Laser Parameters on Topography and Surface Quality. *Dent. Mater.* **2017**, *33*, e28–e38. [[CrossRef](#)]
52. Roitero, E.; Lasserre, F.; Roa, J.J.; Anglada, M.; Mücklich, F.; Jiménez-Piqué, E. Nanosecond-Laser Patterning of 3Y-TZP: Damage and Microstructural Changes. *J. Eur. Ceram. Soc.* **2017**, *37*, 4876–4887. [[CrossRef](#)]
53. Roitero, E.; Anglada, M.; Mücklich, F.; Jiménez-Piqué, E. Mechanical Reliability of Dental Grade Zirconia after Laser Patterning. *J. Mech. Behav. Biomed. Mater.* **2018**, *86*, 257–263. [[CrossRef](#)]
54. Morales, M.; García-González, S.; Rieux, J.; Jiménez-Piqué, E. Nanosecond Pulsed Laser Surface Modification of Yttria Doped Zirconia for Solid Oxide Fuel Cell Applications: Damage and Microstructural Changes. *J. Eur. Ceram. Soc.* **2023**, *43*, 3396–3403. [[CrossRef](#)]
55. Alenazey, F.; Alyousef, Y.; Brancaccio, E.; Montinaro, D. Parameters Affecting CO₂ Production in a Planar Anode Supported SOFC Based System. *Int. J. Hydrogen Energy* **2015**, *40*, 642–651. [[CrossRef](#)]

56. Alenazey, F.; Alyousef, Y.; Almisned, O.; Almutairi, G.; Ghouse, M.; Montinaro, D.; Ghigliazza, F. Production of Synthesis Gas (H_2 and CO) by High-Temperature Co-Electrolysis of H_2O and CO_2 . *Int. J. Hydrogen Energy* **2015**, *40*, 10274–10280. [[CrossRef](#)]
57. Oliver, W.C.; Pharr, G.M. Measurement of Hardness and Elastic Modulus by Instrumented Indentation: Advances in Understanding and Refinements to Methodology. *J. Mater. Res.* **2004**, *19*, 3–20. [[CrossRef](#)]
58. Marquardt, T.; Hollmann, J.; Gimpel, T.; Schade, W.; Kabelac, S. Femtosecond Laser-Induced Surface Modification of the Electrolyte in Solid Oxide Electrolysis Cells. *Energies* **2020**, *13*, 6562. [[CrossRef](#)]
59. Zhu, W.; Nakashima, S.; Marin, E.; Gu, H.; Pezzotti, G. Microscopic Mapping of Dopant Content and Its Link to the Structural and Thermal Stability of Yttria-Stabilized Zirconia Polycrystals. *J. Mater. Sci.* **2020**, *55*, 524–534. [[CrossRef](#)]
60. Parmigiani, F.; Depero, L.E.; Sangaletti, L.; Samoggia, G. An XPS Study of Yttria-Stabilised Zirconia Single Crystals. *J. Electron Spectros. Relat. Phenomena* **1993**, *63*, 1–10. [[CrossRef](#)]
61. Lu, Q.H.; Huang, R.; Wang, L.S.; Wu, Z.G.; Li, C.; Luo, Q.; Zuo, S.Y.; Li, J.; Peng, D.L.; Han, G.L.; et al. Thermal Annealing and Magnetic Anisotropy of NiFe Thin Films on N+-Si for Spintronic Device Applications. *J. Magn. Magn. Mater.* **2015**, *394*, 253–259. [[CrossRef](#)]
62. Kalita, C.; Sarkar, R.D.; Verma, V.; Bharadwaj, S.K.; Kalita, M.C.; Boruah, P.K.; Das, M.R.; Saikia, P. Bayesian Modeling Coherenced Green Synthesis of NiO Nanoparticles Using Camellia Sinensis for Efficient Antimicrobial Activity. *Bionanoscience* **2021**, *11*, 825–837. [[CrossRef](#)]
63. Cabello, A.; Gayán, P.; García-Labiano, F.; De Diego, L.F.; Abad, A.; Izquierdo, M.T.; Adánez, J. Relevance of the Catalytic Activity on the Performance of a NiO/CaAl₂O₄ Oxygen Carrier in a CLC Process. *Appl. Catal. B Environ.* **2014**, *147*, 980–987. [[CrossRef](#)]
64. Grosvenor, A.P.; Biesinger, M.C.; Smart, R.S.C.; McIntyre, N.S. New Interpretations of XPS Spectra of Nickel Metal and Oxides. *Surf. Sci.* **2006**, *600*, 1771–1779. [[CrossRef](#)]
65. Ji, S.; Kim, S.K.; Choi, S.H.; Byun, J.S.; Kim, D.K.; Lee, H.J.; Choi, H.M.; Song, W.; Myung, S.; Suk, J.; et al. Yttria-Stabilized Zirconia Nanoparticles Carbon Nanotube Composite as a Polysulfide-Capturing Lithium-Sulfur Battery Separator. *ACS Appl. Energy Mater.* **2022**, *5*, 12196–12205. [[CrossRef](#)]
66. Luo, S.; Li, X.; Wang, M.; Zhang, X.; Gao, W.; Su, S.; Liu, G.; Luo, M. Long-term electrocatalytic N₂ fixation by MOF-derived Y-stabilized ZrO₂: An insight into deactivation mechanism. *J. Mater. Chem. A.* **2020**, *8*, 5647–5654. [[CrossRef](#)]
67. Roa, J.J.; Ruiz-Morales, J.C.; Canales-Vazquez, J.; Morales, M.; Capdevila, X.G.; Nuñez, P.; Segarra, M. Mechanical characterisation at nanometric scale of a new design of SOFCs. *Fuel Cells* **2011**, *11*, 124–130. [[CrossRef](#)]
68. Xiang, Z.; Fenghui, W.; Jianye, H.; Tiejun, L. Determining the mechanical properties of solid oxide fuel cell by an improved work of indentation approach. *J. Power Sources* **2012**, *201*, 231–235. [[CrossRef](#)]

Disclaimer/Publisher’s Note: The statements, opinions and data contained in all publications are solely those of the individual author(s) and contributor(s) and not of MDPI and/or the editor(s). MDPI and/or the editor(s) disclaim responsibility for any injury to people or property resulting from any ideas, methods, instructions or products referred to in the content.